

Symmetry protected 1D chains in mixed-valence iron oxides

Denis M. Vasiukov,^{1,*} Ghanashyam Khanal,² Ilya Kупenko,³ Georgios Aprilis,⁴
Sergey V. Ovsyannikov,⁵ Stella Chariton,⁵ Valerio Cerantola,⁴ Vasily Potapkin,⁵
Aleksandr I. Chumakov,⁴ Leonid Dubrovinsky,⁵ Kristjan Haule,² and Elizabeth Blackburn¹

¹*Division of Synchrotron Radiation Research, Department of Physics,
Lund University, Box 118, Lund 221 00, Sweden*

²*Department of Physics and Astronomy,
Rutgers University, Piscataway, New Jersey 08854, USA*

³*Institut für Mineralogie, University of Münster,
Corrensstr. 24, 48149 Münster, Germany*

⁴*ESRF, The European Synchrotron, 71 Avenue des Martyrs,
CS40220, 38043 Grenoble Cedex 9, France*

⁵*Bayerisches Geoinstitut, Universität Bayreuth,
Universitätsstr. 30, D-95447 Bayreuth, Germany*

(Dated: July 29, 2022)

Abstract

During the last decade of high-pressure research a whole new series of iron oxides was discovered, like Fe_4O_5 , Fe_5O_6 , Fe_7O_9 etc. [1–6], featuring closely related structures with arrays of one-dimensional (1D) chains of trigonal prisms embedded between slabs of octahedra. Here, we develop a unified approach to the series based on a specific crystallographic generation mechanism which predicts the structures of these oxides and naturally classifies them in terms of the slab cycle. When including magnetic interactions, we show that the 1D chains have a symmetry protection against magnetic perturbations from the iron ions in the slabs, and that the slab size determines the type of magnetic order, which is either ferromagnetic or antiferromagnetic. Dynamical mean-field theory calculations reveal the orbitally selective Mott state of the Fe ions and tendency of conductivity to low-dimensional behavior with particular enhancement along the 1D chains. Across the series, the decoupling of the chains increases, and so with the inherent charge ordering of the slabs, these structures have the potential to allow experimental realization of the model system of coupled 1D wires [7–11]. We point out the possibility to stabilize these compounds in the thin-film form that, together with a wide range of possible ionic substitutions and fact that these compounds are recoverable at ambient pressure, makes them a very promising platform to engineer physical systems with interesting magnetotransport phenomena, as corroborated by the recent discovery of quantum Hall effect in ZrTe_5 [12].

Of the many new high-pressure iron oxides discovered during the last decade, the set consisting of Fe_4O_5 , Fe_5O_6 , HP- Fe_3O_4 etc. [1–6] is particularly special. The oxides in this set share a common packing motif and can be united into a $n\text{FeO}\cdot m\text{Fe}_2\text{O}_3$ homologous series⁴. Many members of this series are recoverable at ambient conditions after high-pressure synthesis and feature iron ions in mixed-valent states^{3,13,14}, resembling magnetite (Fe_3O_4), where this electronic state results in the famous metal-insulator Verwey transition at low temperatures¹⁵, with formation of a peculiar charge-ordered ground state with trimer units of iron ions^{16,17}. Indeed, similar Verwey-type transitions were found in Fe_5O_6 [18] and Fe_4O_5 [13 and 19].

In this paper we focus on an overlooked feature of these compounds, namely that part of the iron ions is arranged in arrays of symmetry protected 1D chains. We use both experimental and computational methods to explore these arrays and argue that, under certain plausible conditions, they could host coupled one-dimensional (1D) wires. Such systems have been extensively studied in theory, but have proven difficult to realize experimentally^{7–11}. These models yield a broad spectrum of fascinating states, from non-Fermi liquid⁷ to a zoo of topological phases^{8–10}, including fractional quantum Hall states, in the case of conductive wires (*viz* Luttinger liquids), and spin liquids in the case of insulating wires¹¹.

We begin with the new insight that stoichiometric variation in the $n\text{FeO}\cdot m\text{Fe}_2\text{O}_3$ series resembles the well-known Magnéli phases²⁰. This motivated us to investigate the underlying crystallographic mechanism responsible for generating the variety of structures seen in this homologous series. There is a close link between the $n\text{FeO}\cdot m\text{Fe}_2\text{O}_3$ series and the ambient pressure $n\text{PbS}\cdot m\text{Bi}_2\text{S}_3$ homologous series, with isostructural correspondence between Fe_5O_6 and the mineral lillianite $\text{Pb}_3\text{Bi}_2\text{S}_6$, and between Fe_5O_7 and PbBi_4S_7 , the so-called V1 phase²¹. This resemblance reveals the common crystallographic generative mechanism behind both series. In the case of the $n\text{PbS}\cdot m\text{Bi}_2\text{S}_3$ series, it was studied in detail and named tropochemical cell-twinning²¹. We illustrate this mechanism in Figure 1 by way of deriving the Fe_4O_5 structure from wüstite (FeO).

The starting point is the parent rocksalt structure of wüstite. If a mirror plane is applied parallel to the $\{311\}$ plane at a sheet of oxygen atoms, we generate a twin. Consecutively applying this operation with some periodic spacing (multiple of d_{311}^{FeO}), we get a new unit cell with identical slabs of the FeO_6 octahedra between twinning planes. As seen from Figure 1, some iron atoms are brought together at the twinning plane upon this procedure.

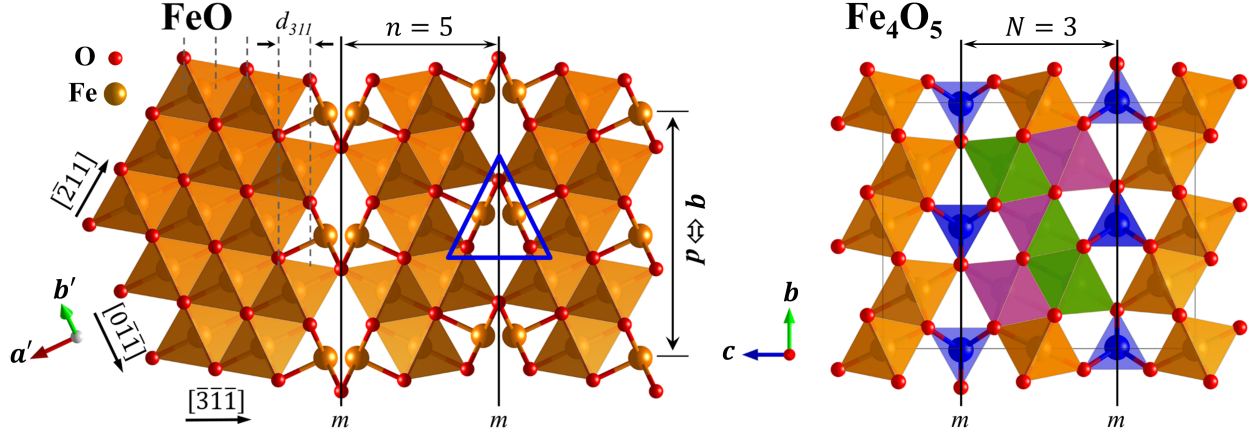


Fig. 1. The $\{311\}$ trochochemical cell-twinning in the homologous series of iron oxides as exemplified by the Fe_4O_5 structure. On the left, the FeO structure is projected along $[0\bar{1}1]$. Regularly applying a mirror plane parallel to (311) at the oxygen sheet at $5d_{311}^{\text{FeO}}$ intervals (slab cycle 3), we derive a structure with a new unit cell. Upon this operation, pairs of iron atoms, as outlined by the blue triangle, are brought into proximity across twinning planes. The last step is the coalescence of these pairs into a single iron atom that leads to a new crystallographic site at the twinning plane with a trigonal prismatic oxygen environment, as marked by the blue colour in the Fe_4O_5 structure on the right. These trigonal prisms form infinite 1D chains along the a axis in the resultant structure. The slab width N can be readily determined using either of two equivalent octahedral chains highlighted by the violet and green cages in the Fe_4O_5 structure. For this particular slab cycle the twinning plane is preserved as a symmetry element in the generated structure. The periodicity p in the plane of projection of FeO is equivalent to the b lattice constant of a new unit cell. Hereafter we use orange and blue colors to designate the octahedral and trigonal prismatic sites respectively.

Merging these atoms gives a new iron site with a trigonal prismatic oxygen environment. The trigonal prisms share common triangular facets and form an array of 1D chains along the a axis separating the octahedral slabs (Fig. 1). This also eliminates iron atoms from the structure, modifying the stoichiometry.

Depending on the spacing between twinning planes, one obtains structures with different slab widths. There are two equivalent ways to define this slab size: (i) the number, n , of d_{311}^{FeO} spacings – in other words the number of the oxygen sheets per slab – and (ii) the number, N , of octahedra in either of the two octahedral chains along $\langle\bar{2}11\rangle$ and $\langle 0\bar{1}\bar{1}\rangle$ directions in the initial wüstite structure. Hereafter we will use the latter notation, but there is a simple

conversion between them, namely $n = N + 2$.

The $\{311\}$ cell-twinning mechanism considered here can eliminate up to one third of the cations from the initial rocksalt structure given the smallest slab width of one octahedron, which corresponds to the η -Fe₂O₃ phase⁴. Variation in stoichiometry leads to changes in the average cation valence state, starting from pure +2 in FeO to pure +3 in η -Fe₂O₃, with the formation of numerous mixed-valence compounds at intermediate stoichiometries.

In Extended Data Table I, the known members of the $n\text{FeO}\cdot m\text{Fe}_2\text{O}_3$ series are collected. It is natural to classify these oxides according to the slab cycle, or sequence of slabs, which entirely determines the symmetry and crystallographic positions in the generated structures. Most of the compounds in Extended Data Table I can be assigned to two groups, the N -family and $N,N+1$ -family. The N -family has the simplest cycle, with only one type of slab, and crystallizes in an orthorhombic space group $Cmcm$ (#63). The mirror plane perpendicular to the c axis in this family is the initial twinning plane as illustrated in Figure 1. There is a subtle crystallographic difference between compounds with even and odd N that has important consequences for the magnetic structure (see Supplementary Materials for details).

The $N,N+1$ -family contains slabs of two different widths differing by one octahedron. This slab cycle does not allow preservation of the twinning plane as a symmetry element in the resulting structures. Instead, only symmetry elements relevant to the a axis of $Cmcm$ space group are preserved, and the unit cell becomes monoclinic with space group $C2/m$ (#12).

Generally speaking the slab cycle can be arbitrarily complex, as seen in the phase-V sub-series of the lillianite structure²¹. The first sign of this complexity in the iron oxides is the recently discovered Fe₇O₁₀ [6], with a trinomial slab cycle 1,1,2 which contains two different twinning planes between the 1,1 and 1,2 slabs, where only the first one is preserved as a mirror plane in the resulting structure. New iron oxides with more complex slab cycle are likely to be discovered in the future.

The representative Mössbauer spectra of the studied oxides are shown in Fig. 2. Their basic feature is the presence of two distinct components. One belongs to the octahedral slab while the other corresponds to the chains of trigonal prisms. The data show that in all recoverable oxides, namely Fe₄O₅, Fe₅O₆ and Fe₇O₉, the chains are exclusively populated by Fe²⁺ ions at ambient conditions. This observation allows us to estimate the average

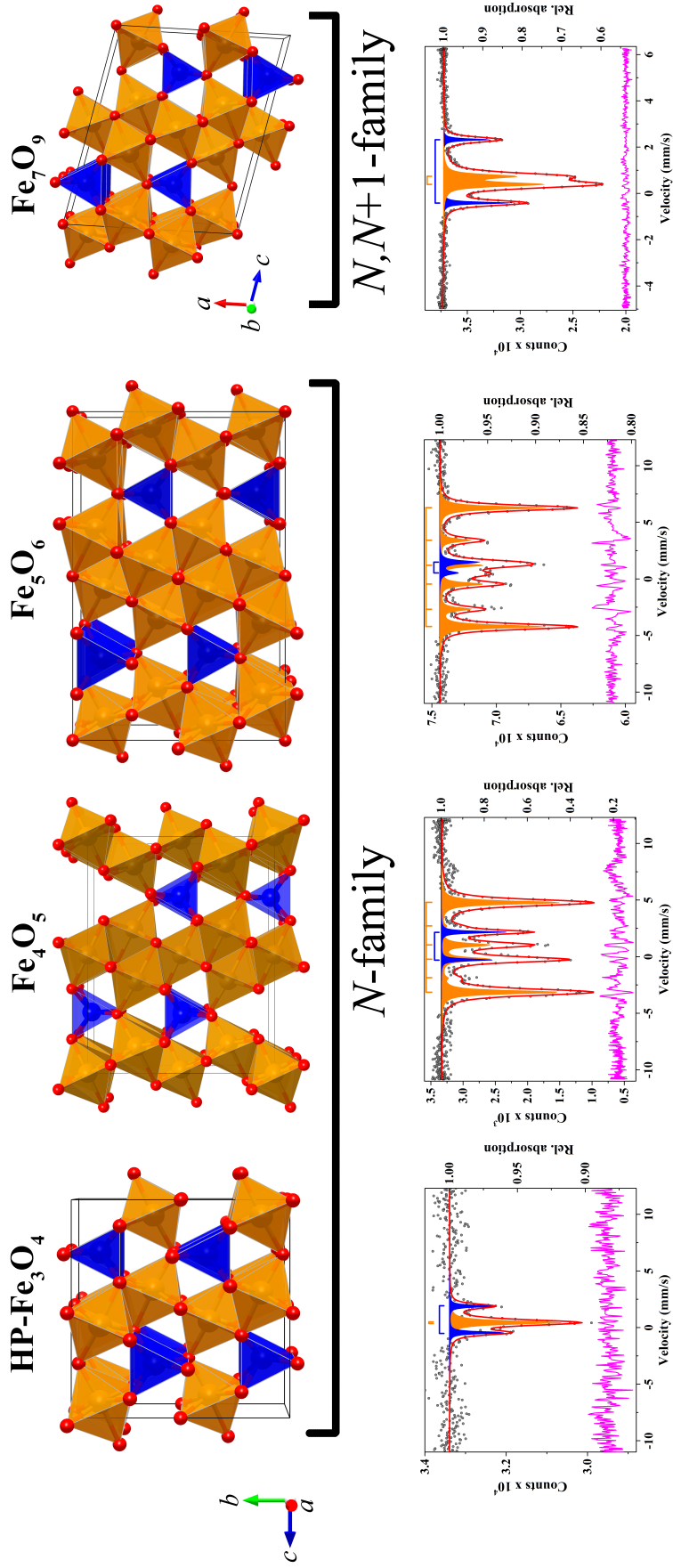


Fig. 2. Mössbauer spectra of several members of the $n\text{FeO} \cdot m\text{Fe}_2\text{O}_3$ homologous series at room temperature. The blue and orange components correspond to iron ions in the trigonal prismatic and octahedral environment, respectively. The pink line is the fit residual. In the paramagnetic region all of these oxides show similar spectra consisting of two distinct doublets corresponding to the iron ions in different oxygen environment, here exemplified by HP-Fe₃O₄ and Fe₇O₉. The spectra of the Fe₄O₅ and Fe₅O₆ oxides show an unexpected coexistence of the magnetic sextet from the octahedral slab with the paramagnetic doublet of the trigonal prismatic site. This means that magnetic ordering in the octahedral slab does not influence iron ions in the chains of trigonal prisms. The spectrum of HP-Fe₃O₄ was collected at 20 GPa whereas other spectra were acquired at ambient pressure; the spectrum of Fe₇O₉ was already published in [3].

oxidation state of the Fe ions in the slabs and the isomer shifts of the slab components are indeed in a good agreement with the predicted values (Extended Data Table II).

An intriguing feature of the spectra in Fig. 2 is the apparent coexistence of the magnetically ordered iron ions in the slabs with the disordered iron ions in the chains of Fe_4O_5 and Fe_5O_6 . Accordingly, we deduce that in both compounds slabs and chains have two different ordering temperatures and that the magnetic ordering of the 1D chains is independent from that of the slabs. This peculiar magnetic behavior was also observed in the isostructural compounds MnFe_3O_5 and CoFe_3O_5 [22 and 23] and it is confirmed to be stable by our theoretical calculations. Thus our data invalidates the previously published model of magnetic structure for Fe_4O_5 [19], where the simultaneous magnetic ordering of all iron ions was assumed.

Among the oxides presented in Fig. 2 the HP- Fe_3O_4 is the only non-recoverable phase and so its spectrum was acquired at 20 GPa, after in situ synthesis in diamond anvil cell. Although HP- Fe_3O_4 , as an $N = 2$ member of the N -family, could, in principle, possess iron ions in an integer oxidation state, our data unexpectedly revealed the presence of mixed-valent states in both crystallographic positions, i.e. in the chains and slabs.

To understand the origin of the independent magnetic behavior of spins in slabs and chains it is instructive to establish a generic scheme of exchange interactions in these structures. Let us consider them for Fe_4O_5 , the $N = 3$ member of the N -family, since in this case there are neutron diffraction data²²⁻²⁴ for several isostructural compounds and solid solutions differing only by cations in the chains (namely Ca, Mn or Co), which revealed an identical collinear antiferromagnetic order of the slabs at room temperature with a (0 0 0) propagation vector presented in Fig. 3a.

In this magnetic structure, the magnetic moments in the slabs align along the c -axis, with ferromagnetic exchange along the a -axis and antiferromagnetic exchange along the b - and c -axis (Fig. 3a). This pattern of exchange interactions in the octahedral slab should be relevant not only in Fe_4O_5 but can be generalized to all members of the N -family. This conjecture is supported by our DMFT calculations for HP- Fe_3O_4 and the data from CaFe_5O_7 , which is equivalent to the $N = 5$ case, where the same magnetic configuration is adopted in the ground state²⁵. As for the chains, application of the well-known Goodenough-Kanamori-Anderson (GKA) rules suggests that they should have relatively weak *intrachain* ferromagnetic coupling in case of Fe^{2+} ions (see Suppl. Materials).

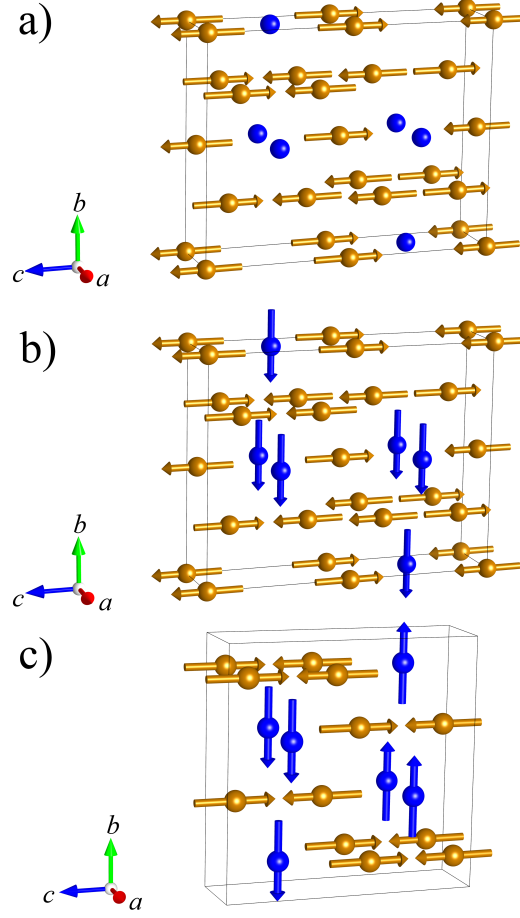


Fig. 3. The expected magnetic configurations for the charge-averaged state in the N -family. The transition from paramagnetic to completely magnetically ordered state proceeds via the intermediate partially ordered state (a), with the magnetically ordered slabs but the disordered 1D chains. The complete magnetic order differs in odd and even N compounds due to the ferromagnetic and antiferromagnetic *interchain* ordering, respectively. We illustrate this here with (b) $N = 3$, i.e. Fe₄O₅, and (c) $N = 2$, i.e. HP-Fe₃O₄, structures.

The fact that ordering in the 1D chains is independent of the ordering in the slabs is due to symmetry protection provided by the preserved twinning plane in the N -family. For the case of the antiferromagnetic structure in Fig. 3a, the induced Weiss fields from magnetically ordered adjacent octahedral slabs exactly cancel out each other for iron atoms located at the mirror plane. Therefore magnetic interactions in the 1D chains are *symmetry-protected* against perturbations from the octahedral slabs and also from the interchain interactions along the c -axis. Consequently, the chains have lower ordering temperatures, as determined

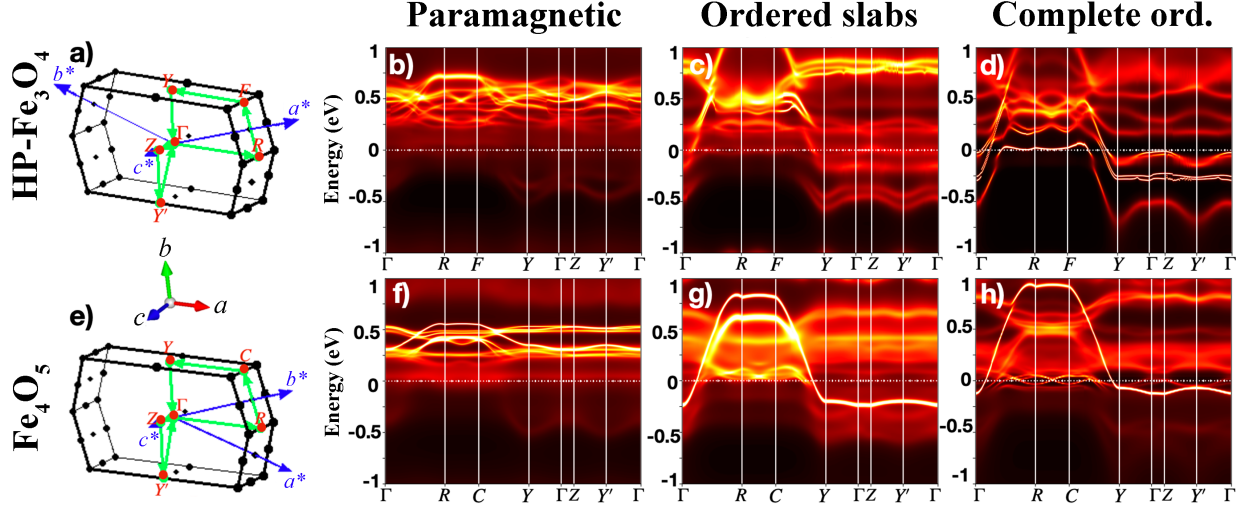


Fig. 4. Theoretical eDMFT spectral functions of HP-Fe₃O₄ (top row) and Fe₄O₅ (bottom row) in three different states: paramagnetic (b and f), partially ordered state with ordered magnetic slabs and disordered chains as in Fig. 3a (c and g) and complete long range ordering established on all Fe atoms as in Fig. 3c and 3b (d and h) in magnetic space groups #63.465 and #63.464, respectively. In a and e the first primitive Brillouin zones are shown with respective momentum pathway used in the plots, and between them the corresponding crystallographic axes are displayed to show the relative orientation of reciprocal space to the real space, namely $\Gamma - R$ is parallel to the a axis, $\Gamma - Y$ is parallel to the b axis and $\Gamma - Z$ is parallel to the c axis.

by the intrachain interactions.

At intermediate temperatures this leads to the peculiar magnetic structure with coexistence of ordered slabs and disordered chains (Fig. 3a) that is observed in our Mössbauer spectra of Fe₄O₅ and Fe₅O₆ at room temperature in Fig. 2. From these observations it immediately follows that such independent magnetic ordering cannot be observed in the monoclinic $N, N+1$ -family. Indeed, in our DMFT simulations for Fe₇O₉ we observe non-zero Weiss field in the chains for all types of magnetic order in the slabs, contrary to Fe₄O₅ and HP-Fe₃O₄ where coexisting magnetic state (Fig. 3a) is found to be stable, with no induced Weiss field in the chains.

Therefore upon complete magnetic ordering for the N -family we expect to see ferromagnetic chains embedded in the antiferromagnetic background of the slabs (Fig. 3b and 3c). The subtle crystallographic difference between odd and even N compounds mentioned above results in ferromagnetic *interchain* ordering in the odd N case (Fig. 3b) and antiferromag-

netic *interchain* ordering in the even N case (Fig. 3c). Thus the odd and even N compounds should have a ferromagnetic and an antiferromagnetic ground state, respectively (see Suppl. Materials for more details).

Ab-initio simulations have been performed by the combination of Density Functional Theory and embedded Dynamical Mean Field Theory (DFT+eDMFT) for two members of the N -family, HP-Fe₃O₄ and Fe₄O₅, i.e. even and odd N case, respectively, in three different states at 120 K: (i) the paramagnetic state with all local moments disordered, (ii) the intermediate partially ordered state with magnetically ordered slabs but disordered 1D chains (Fig. 3a), and (iii) the state with complete magnetic order on all Fe atoms (Fig. 3b and 3c).

In accordance with the expected mixed-valent state, both compounds are metallic in all three magnetic configurations. Overall our results are consistent with previous paramagnetic (DFT+eDMFT) calculations of Fe₄O₅ and Fe₅O₆ [26 and 27] and the computed oxidation states of Fe atoms are in good agreement with our Mössbauer data (see occupation number n_d in Extended Data Table III).

The obtained single-particle spectral functions are displayed in Fig. 4. Fe atoms in the slabs are coordinated by the oxygen octahedra, hence the t_{2g} orbitals are lower in energy and are partially occupied with finite density of states at the Fermi level, whereas the e_g orbitals are almost exactly half-filled, and are fully gapped with the large Mott gap exceeding 1 eV, see Extended Data Fig. 5 and 6. In the 1D chains, the Fe atoms are sitting in trigonal prisms (see Suppl. Materials for the orbital splitting in the trigonal prism), and here the z^2 and $x^2 - y^2$ orbitals appear metallic, while the other three orbitals are gapped.

The divergent self-energy, seen as sharp poles in Extended Data Fig. 5 and 6, attests to the Mott insulating nature of the gapped orbitals, and shows enormous scattering rate values for them. This implies that the Fe atoms in the paramagnetic state appear in a very unusual configuration, namely the orbitally selective Mott state^{28–39}, which is well known for its bad metallic behaviour. The Mott-insulating localized electrons provide a strong source of spin scattering for the electrons in the metallic orbitals, and so the latter cannot properly conduct electrons³¹. Perhaps the most famous example of such selective Mott states are the colossal magnetoresistive manganites^{40,41}, but several other systems were recently studied as potential candidates to harbor such unusual electronic configurations^{28,34,35,39}. Due to this large spin scattering, the spectral functions of these paramagnetic states (Fig. 4b and 4f)

are very diffuse and show no evidence for developed conducting bands around the Fermi level. The predicted electrical conductivity at 100 K is of the order of 10^5 S/m and is rather isotropic (see the Extended Data Table III).

Upon magnetic ordering of the slabs, the spin-scattering on octahedrally coordinated Fe atoms is arrested, and so the electrons on these atoms experience very small scattering rates. The metallic orbitals now start to form bands which cross the Fermi level (see Fig. 4c and 4g), but these bands are still relatively fuzzy, because the spin scattering in the chains remains active. The plot of the density of states and the scattering rate in Extended data Figs. 5 and 6 confirm that not much has changed for the Fe atoms in the chains, even though the slabs are now magnetically ordered. Consequently, the conductivity has increased by approximately a factor of two (see Extended Data Table III), but it is still quite isotropic and small for a metallic system.

Finally the magnetic moments in the chains also order, as depicted in Fig. 3b and 3c, which removes all spin scattering at the Fermi level, making the system a normal magnetic metal with sharp bands near the Fermi level, as shown in Fig. 4d and 4h. This state shows the peculiar tendency to low-dimensional behavior, namely the strong dispersion of the bands along the $\Gamma - R$ and $F(C) - Y$ direction of the first Brillouin zone, as shown in Fig. 4a and 4e, while along the orthogonal directions the bands are mostly flat. The first direction is along the 1D chains of trigonal prisms, i.e. the real space a axis, therefore we expect enhanced conductivity along the 1D chains.

Indeed, the calculation results in Extended Data Table III show increased anisotropic conductivity with largest values along the chains in this ordered state. In HP-Fe₃O₄ conductivity increases by an order of magnitude and the anisotropy ($2\sigma^a/[\sigma^b + \sigma^c]$) is about two, although we find that it is very sensitive to doping and can become as large as five upon a small shift of the Fermi level (see Extended Data Table IV).

It is interesting to note that in the completely ordered magnetic state of HP-Fe₃O₄ the flat parts of the bands at the Fermi level are mostly formed by the z^2 and $x^2 - y^2$ orbitals of the Fe atoms in the 1D chains, as evident by the narrow peak in the corresponding densities of states at the Fermi level (see Extended Data Fig. 5). Therefore, the chains show a clear tendency to act as an 1D conductors.

Up to now we have treated these compounds only in the charge-averaged state. However, at low temperatures the inherent mixed-valence state of the slabs can act as a natural switch

between metallic and insulating behavior by means of the charge-ordering transition^{18,19}. This means that the anisotropy could be enhanced even further in the true charge-ordered ground state, leaving the arrays of chains as the only conductive channel at low temperature.

The N -family is therefore a 3D system with an emergent dimensionality reduction. This is brought about because the tropochemical cell-twinning mechanism magnetically isolates the iron ions in the trigonal prisms from the surrounding slabs, allowing the 1D nature of the chains to manifest in physical properties like the conductivity. This conclusion is rather general and this symmetry protection of magnetic interactions in the chains also applies under ionic substitution^{22,23} and in other examples even with the $(1/2\ 0\ 0)$ magnetic propagation vector, as in stoichiometric CaFe_3O_5 [42].

Crucially, these materials are transferable to the ambient pressure realm, as distinct to the superconducting high-pressure hydrides⁴³. Half of the oxides listed in Extended Data Table III are recoverable and, in addition, these structures show great compositional flexibility that considerably affects their stability field^{44–46}. For instance, compounds with $N \geq 3$ can be synthesized *even at ambient pressure* if the Fe atoms in the chains are substituted by Ca [47 and 48] while another interesting alternative is to substitute oxygen with other chalcogens, as exemplified by the lillianite case²¹.

Furthermore, the crystallographic derivation mechanism described here suggests that it may be possible to stabilize these compounds in the thin-film form. The inherent connection with the rock salt structure via tropochemical cell-twinning (Fig. 1) means that (011)-oriented substrates with rock salt structure could provide a coherent interface for the (100)-oriented films of the N -family members.

To conclude, the distinct magnetic and electronic properties of the structures in this series make them candidates for the realization of a large variety of interesting physical systems, particularly considering magnetoresistance. One possible implementation should be highlighted, namely the coupled quantum wire models^{7–11}, because the arrays of conductive 1D chains described here would be an excellent testbed for them. However the range of possible phenomena is much wider and the recent observation of the 3D quantum Hall effect in ZrTe_5 [12] confirm this, as it is equivalent to the $N = 3$ member of N -family with empty cationic sites in the slabs.

Acknowledgements We are grateful to Daniel I. Khomskii and Pavel A. Volkov for inspiring discussions. D.V. and E.B. thank the Swedish Research Council for support under grant number 2018-04704. G.K. and K.H. acknowledge the support of National Science Foundation by the grant number DMR-1709229. We acknowledge the European Synchrotron Radiation Facility for provision of synchrotron radiation resources at the beamline ID18.

Author contributions S.O., L.D. and D.V. prepared the samples. D.V., I.K., G.A., S.C., V.C., V.P., L.D. and A.C. performed the Mössbauer experiments. G.K. and K.H. performed the DFT+eDMFT calculations. D.V. developed the crystallographic approach. D.V., K.H. and E.B. interpreted the results and wrote the manuscript with input from all co-authors.

METHODS

Sample preparation The single crystals of Fe_4O_5 and Fe_5O_6 were synthesized in a 1200-tonne multi-anvil press at the Bavarian Research Institute of Experimental Geochemistry and Geophysics (BGI) at 14-16 GPa and 1200-1400 °C from the stoichiometric mixtures of Fe_3O_4 (Aldrich, 99.99% purity) and Fe (99.99%). The details of the synthesis were described in previous works^{13,18}. For the Mössbauer experiments we selected single crystals using a three-circle Bruker diffractometer equipped with a SMART APEX CCD detector and a high-brilliance Rigaku rotating anode (Rotor Flex FR-D, Mo- K_α radiation) with Osmic focusing X-ray optics.

To obtain well-crystallized pure HP- Fe_3O_4 phase we performed an *in situ* synthesis in a BX90 diamond anvil cell⁴⁹ (DAC) using laser heating at 20 GPa from a magnetite single crystal enriched with ^{57}Fe . We used a double-sided laser-heating system with infrared lasers^{50,51}. The phase transition from spinel structure to the high-pressure phase was clearly seen from Mössbauer spectra as at this pressure the spinel phase has two well-developed magnetic sextets while the spectrum of HP- Fe_3O_4 is a superposition of two paramagnetic doublets.

Mössbauer spectroscopy The Mössbauer spectra were collected at the Nuclear Resonance beamline⁵² (ID18) at the European Synchrotron Radiation Facility (ESRF) using the synchrotron Mössbauer source (SMS)⁵³. The SMS is based on a high-quality single crys-

tal of $^{57}\text{FeBO}_3$ which acts as a nuclear monochromator. Energy modulation is achieved by means of a standard Mössbauer velocity transducer on which the borate crystal is mounted. The advantages of SMS are the small beam spot size, about 10–15 μm , and the absence of non-resonant radiation that greatly improves the data quality and decreases the acquisition time for experiments with DACs.

The folded Mössbauer spectra contain 512 channels and were fitted using the MossA software⁵⁴, version 1.01a. We used a transmission integral fit assuming a Lorentzian-squared line shape of the SMS and a Lorentzian or pseudo-Voigt line shape for the absorber. The line width and the center shift of the SMS was controlled before and after collection of each spectrum using the reference single line absorber ($\text{K}_2\text{Mg}^{57}\text{Fe}(\text{CN})_6$). All center shifts are reported relative to $\alpha\text{-Fe}$ at ambient conditions.

The assignment of the oxidation state of iron ions was done based on the comparison of the determined isomer shift values with literature data of high-spin iron ions in oxygen environment⁵⁵. As a reference for the 6-fold oxygen coordinated iron at ambient pressure we took values of octahedral $\text{Fe}^{2.5+}$ in magnetite (0.67 mm/s) and Fe^{3+} in hematite (0.36 mm/s), to minimize the influence of the inductive effect⁵⁵. The isomer shift of the iron ion in the +2.5 mixed-valent state is just an average of the isomer shifts of pure divalent and trivalent iron. Therefore from the magnetite value it follows that pure Fe^{2+}O_6 would have 0.98 mm/s isomer shift and this allows us to calculate the isomer shift for iron ions in any intermediate oxidation state between +2 and +3. As can be seen from Extended Data Table II the iron ions in the trigonal prisms of Fe_4O_5 , Fe_5O_6 and Fe_7O_9 oxides have isomer shifts very close to our estimate, confirming occupation of the trigonal prismatic sites by pure Fe^{2+} . Under this assumption we can calculate the average oxidation state of iron ions in the octahedral slabs and in the same manner predict isomer shift values for them. In Extended data Table II one can see a remarkable agreement between experimental and predicted values.

The spectrum of $\text{HP-Fe}_3\text{O}_4$ was collected after synthesis at 20 GPa so we need to make a correction for the pressure dependence of isomer shift which we thoroughly studied in our previous work⁵⁶. Although from the stoichiometry of $\text{HP-Fe}_3\text{O}_4$ one would expect only pure Fe^{2+} and Fe^{3+} in the chains and slabs, respectively, the determined isomer shift values are quite far away from the expected numbers (Extended Data Table II). Note that the deviation from the calculated number is opposite for the chains and slabs, which corresponds to an admixture of trivalent iron to the chains and divalent iron to the slabs. Therefore the mixed-

valent state is adapted by both crystallographic positions in this phase. The results of our DMFT calculations in Extended Data Table III also show a similar trend.

DFT+eDMFT calculations The theoretical calculations were carried out by the combination of DFT and eDMFT⁵⁷, as implemented in WIEN2k and the Rutgers eDMFT code^{58–60}. These calculations are charge self-consistent and use exact double-counting between DFT and DMFT⁶¹. For the self-consistent calculation we set RK_{max} (which determines the size of basis) to be 7.0 and used 1000 k -points for the k -point sampling in the irreducible Brillouin zone. To compute the resistivity, we used up to 10000 k -points. We adopted the local-density approximation (LDA)⁶², which gives the best results for lattice properties when combined with eDMFT⁶³. The self-energy on the real axis was obtained using the analytical continuation by maximum entropy method. The experimental crystal structures used in calculations were taken from works [1 and 4], namely Fe_4O_5 at 10 GPa and HP- Fe_3O_4 at 44 GPa. We used $U=10.0$ eV and $J_H = 1.0$ eV for the Coulomb repulsion and Hund’s coupling respectively, as obtained by the constrained DMFT calculation. The auxiliary impurity problem was solved using a continuous-time quantum Monte Carlo impurity solver⁶⁴.

The magnetic structures were first guessed by finding the Weiss field on each Fe atom in the presence of the exchange field of the neighboring Fe atoms, which can provide several candidate orderings which can be further simulated for their stability. Among several trial configurations, we found that the theoretical ordering of Fe magnetic moments, depicted in Fig. 3, is indeed energetically favourable to other configurations.

Note that the spin configurations used in calculations (Extended Data Figs. 7 and 8) are non-collinear, and canted along the high-symmetry axis of the octahedra, which minimizes the sign problem in quantum Monte Carlo. Namely, in the DMFT calculation the local coordinate axis is chosen such that it coincides with the high symmetry axis of the polyhedron, which minimizes the non-diagonal hybridization, and hence reduces the sign problem. The spin-orientation along the z -axis then does not introduce additional off-diagonal hybridization, which makes the sign problem in magnetic calculation approximately equal to the paramagnetic case.

Extended data Table III shows the Fe occupation numbers n_d . In this work, the DMFT calculations were carried out in the complete Linear Augmented Plane Wave basis, and the occupation numbers were computed by integrating the electronic charge within the touching

Muffin-tin spheres around iron atoms and projecting them to the relevant d orbitals.

The theoretical conductivity in the same table was calculated as the zero frequency limit of the optical conductivity, which is computed as the convolution of the single-particle Green's functions with the proper velocity matrix elements. Notice that the vertex corrections to conductivity vanish within the single site eDMFT framework because considered here structure have the inversion symmetry. All visualizations of crystal and magnetic structures in this work were prepared using the VESTA software⁶⁵.

* vasiukov.dv@gmail.com

- ¹ Lavina, B. *et al.* Discovery of the recoverable high-pressure iron oxide Fe_4O_5 . *Proc. Natl. Acad. Sci.* **108**, 17281–17285 (2011).
- ² Lavina, B. & Meng, Y. Unraveling the complexity of iron oxides at high pressure and temperature: Synthesis of Fe_5O_6 . *Sci. Adv.* **1**, e1400260 (2015).
- ³ Sinmyo, R. *et al.* Discovery of Fe_7O_9 : a new iron oxide with a complex monoclinic structure. *Sci. Rep.* **6**, 32852 (2016).
- ⁴ Bykova, E. *et al.* Structural complexity of simple Fe_2O_3 at high pressures and temperatures. *Nat. Commun.* **7** (2016).
- ⁵ Ishii, T., Uenver-Thiele, L., Woodland, A. B., Alig, E. & Ballaran, T. B. Synthesis and crystal structure of Mg-bearing Fe_9O_{11} : New insight in the complexity of Fe-Mg oxides at conditions of the deep upper mantle. *Am. Mineral.* **103**, 1873–1876 (2018).
- ⁶ Koemets, E. *et al.* Chemical stability of FeOOH at high pressure and temperature, and oxygen recycling in early Earth history. *Eur. J. Inorg. Chem.* **2021**, 3048–3053 (2021).
- ⁷ Vishwanath, A. & Carpentier, D. Two-dimensional anisotropic non-Fermi-liquid phase of coupled Luttinger liquids. *Phys. Rev. Lett.* **86**, 676 (2001).
- ⁸ Kane, C., Mukhopadhyay, R. & Lubensky, T. Fractional quantum Hall effect in an array of quantum wires. *Phys. Rev. Lett.* **88**, 036401 (2002).
- ⁹ Teo, J. C. & Kane, C. From Luttinger liquid to non-Abelian quantum Hall states. *Phys. Rev. B* **89**, 085101 (2014).
- ¹⁰ Iadecola, T., Neupert, T., Chamon, C. & Mudry, C. Wire constructions of Abelian topological phases in three or more dimensions. *Phys. Rev. B* **93**, 195136 (2016).

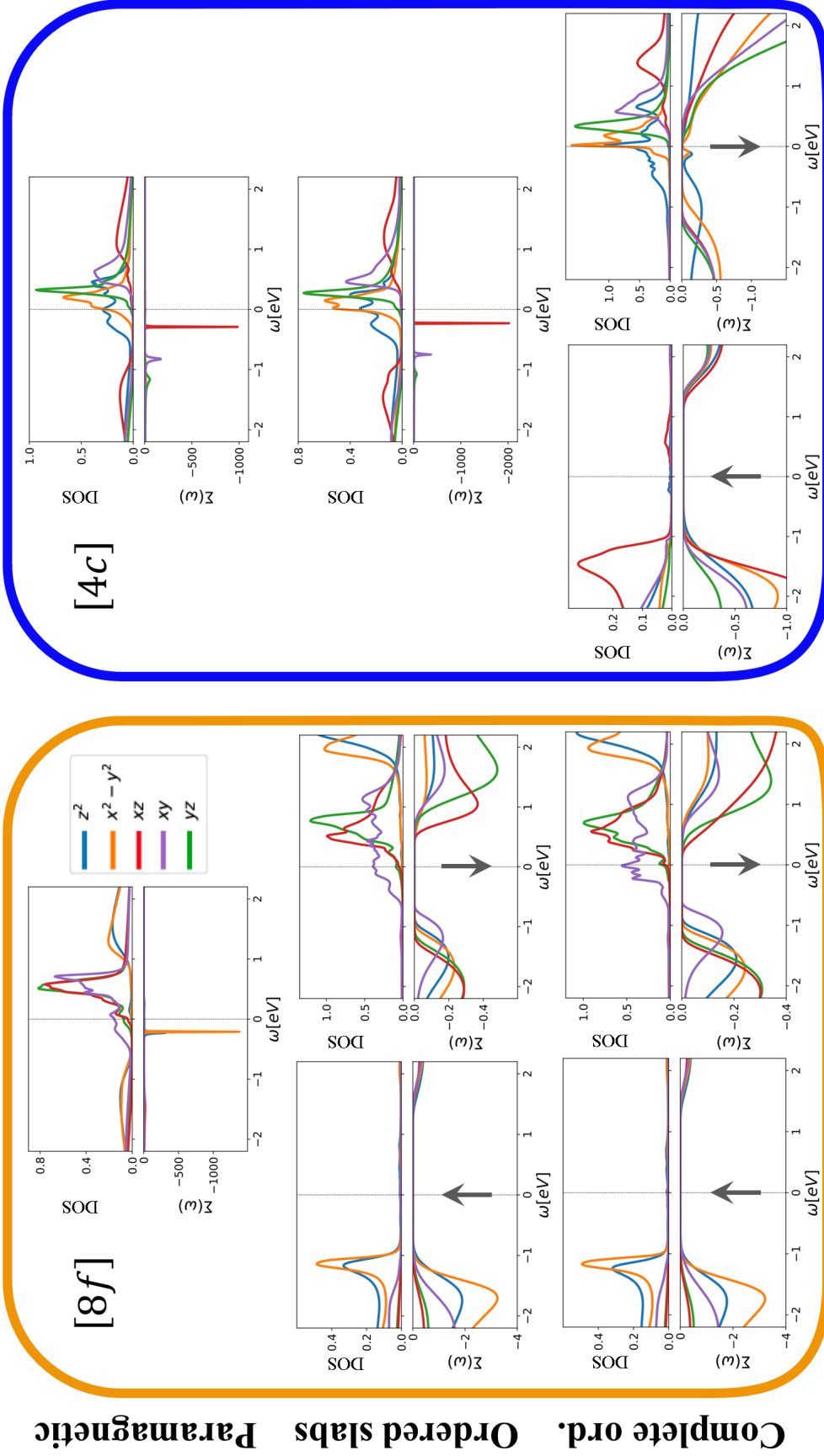
- ¹¹ Meng, T., Neupert, T., Greiter, M. & Thomale, R. Coupled-wire construction of chiral spin liquids. *Phys. Rev. B* **91**, 241106 (2015).
- ¹² Tang, F. *et al.* Three-dimensional quantum Hall effect and metal–insulator transition in ZrTe_5 . *Nature* **569**, 537–541 (2019).
- ¹³ Ovsyannikov, S. V. *et al.* Pressure tuning of charge ordering in iron oxide. *Nat. Commun.* **9**, 4142 (2018).
- ¹⁴ Maitani, S., Sinmyo, R., Ishii, T., Kawaguchi, S. I. & Hirao, N. The electrical conductivity of Fe_4O_5 , Fe_5O_6 , and Fe_7O_9 up to 60 GPa. *Phys. Chem. Miner.* **49**, 1–8 (2022).
- ¹⁵ Verwey, E. Electronic conduction of magnetite (Fe_3O_4) and its transition point at low temperatures. *Nature* **144**, 327–328 (1939).
- ¹⁶ Senn, M. S., Wright, J. P. & Attfield, J. P. Charge order and three-site distortions in the Verwey structure of magnetite. *Nature* **481**, 173–176 (2012).
- ¹⁷ Baldini, E. *et al.* Discovery of the soft electronic modes of the trimeron order in magnetite. *Nat. Phys.* (2020).
- ¹⁸ Ovsyannikov, S. V. *et al.* Room-temperature Verwey-type transition in iron oxide, Fe_5O_6 . *Angew. Chem., Int. Ed.* **59**, 5632–5636 (2020).
- ¹⁹ Ovsyannikov, S. V. *et al.* Charge-ordering transition in iron oxide Fe_4O_5 involving competing dimer and trimer formation. *Nat. Chem.* **8**, 501 (2016).
- ²⁰ Schwingenschlögl, U. & Eyert, V. The vanadium Magnéli phases $\text{V}_n\text{O}_{2n-1}$. *Ann. Phys.* **13**, 475–510 (2004).
- ²¹ Takèuchi, Y. *Tropochemical Cell-twinning: A Structure-building Mechanism in Crystalline Solids*. Material science of minerals and rocks (Terra Scientific Pub., 1997).
- ²² Hong, K. H., Arevalo-Lopez, A., Coduri, M., McNally, G. & Attfield, J. P. Cation, magnetic, and charge ordering in MnFe_3O_5 . *J. Mater. Chem. C* **6**, 3271–3275 (2018).
- ²³ Hong, K. H., Solana-Madruga, E., Coduri, M. & Attfield, J. P. Complex cation and spin orders in the high-pressure ferrite CoFe_3O_5 . *Inorg. Chem.* **57**, 14347–14352 (2018).
- ²⁴ Hong, K. H., Arevalo-Lopez, A. M., Cumby, J., Ritter, C. & Attfield, J. P. Long range electronic phase separation in CaFe_3O_5 . *Nat. Commun.* **9**, 2975 (2018).
- ²⁵ Delacotte, C. *et al.* Morin-like spin canting in the magnetic CaFe_5O_7 ferrite: a combined neutron and Mössbauer study. *J. Solid State Chem.* **247**, 13–19 (2017).
- ²⁶ Yang, A. *et al.* Metallic nature and site-selective magnetic moment collapse in iron oxide Fe_4O_5

- at the extreme conditions of Earth’s deep interior. *Phys. Lett. A* **414**, 127607 (2021).
- ²⁷ Qin, Q.-Y. *et al.* Site-selective magnetic moment collapse in compressed Fe_5O_6 . *Chin. Phys. Lett.* **38**, 089101 (2021).
- ²⁸ Anisimov, V., Nekrasov, I., Kondakov, D., Rice, T. & Sigrist, M. Orbital-selective Mott-insulator transition in $\text{Ca}_{2-x}\text{Sr}_x\text{RuO}_4$. *Eur. Phys. J. B* **25**, 191–201 (2002).
- ²⁹ Koga, A., Kawakami, N., Rice, T. & Sigrist, M. Orbital-selective Mott transitions in the degenerate Hubbard model. *Phys. Rev. Lett.* **92**, 216402 (2004).
- ³⁰ Koga, A., Kawakami, N., Rice, T. & Sigrist, M. Spin, charge, and orbital fluctuations in a multiorbital Mott insulator. *Phys. Rev. B* **72**, 045128 (2005).
- ³¹ Biermann, S., de’ Medici, L. & Georges, A. Non-Fermi-liquid behavior and double-exchange physics in orbital-selective Mott systems. *Phys. Rev. Lett.* **95**, 206401 (2005).
- ³² Liebsch, A. Novel Mott transitions in a nonisotropic two-band Hubbard model. *Phys. Rev. Lett.* **95**, 116402 (2005).
- ³³ Werner, P. & Millis, A. J. High-spin to low-spin and orbital polarization transitions in multiorbital Mott systems. *Phys. Rev. Lett.* **99**, 126405 (2007).
- ³⁴ de’ Medici, L., Hassan, S. R., Capone, M. & Dai, X. Orbital-selective Mott transition out of band degeneracy lifting. *Phys. Rev. Lett.* **102**, 126401 (2009).
- ³⁵ Vojta, M. Orbital-selective Mott transitions: Heavy fermions and beyond. *J. Low Temp. Phys.* **161**, 203–232 (2010).
- ³⁶ Huang, L., Wang, Y. & Dai, X. Pressure-driven orbital selective insulator-to-metal transition and spin-state crossover in cubic CoO . *Phys. Rev. B* **85**, 245110 (2012).
- ³⁷ Herbrych, J. *et al.* Spin dynamics of the block orbital-selective Mott phase. *Nat. Commun.* **9**, 1–10 (2018).
- ³⁸ Herbrych, J., Alvarez, G., Moreo, A. & Dagotto, E. Block orbital-selective Mott insulators: a spin excitation analysis. *Phys. Rev. B* **102**, 115134 (2020).
- ³⁹ Kim, M., Kim, H.-S., Haule, K. & Vanderbilt, D. Orbital-selective Mott phase and non-Fermi liquid in FePS_3 . *Phys. Rev. B* **105**, L041108 (2022).
- ⁴⁰ Tokura, Y. & Tomioka, Y. Colossal magnetoresistive manganites. *J. Magn. Magn. Mater.* **200**, 1–23 (1999).
- ⁴¹ Pascut, G. L. & Haule, K. Role of orbital selectivity on crystal structures and electronic states in BiMnO_3 and LaMnO_3 perovskites. *arXiv preprint arXiv:2005.12179* (2020).

- ⁴² Cassidy, S. J., Orlandi, F., Manuel, P. & Clarke, S. J. Single phase charge ordered stoichiometric CaFe_3O_5 with commensurate and incommensurate trimeron ordering. *Nat. Commun.* **10** (2019).
- ⁴³ Pickard, C. J., Errea, I. & Erements, M. I. Superconducting hydrides under pressure. *Annu. Rev. Condens. Matter Phys.* **11**, 57–76 (2020).
- ⁴⁴ Woodland, A. *et al.* Fe_4O_5 and its solid solutions in several simple systems. *Contrib. Mineral. Petrol.* **166**, 1677–1686 (2013).
- ⁴⁵ Boffa Ballaran, T., Uenver-Thiele, L. & Woodland, A. B. Complete substitution of Fe^{2+} by Mg in Fe_4O_5 : The crystal structure of the $\text{Mg}_2\text{Fe}_2\text{O}_5$ end-member. *Am. Mineral.* **100**, 628–632 (2015).
- ⁴⁶ Hong, K. H. *Synthesis and properties of CaFe_3O_5 and related materials*. Ph.D. thesis, The University of Edinburgh (2019).
- ⁴⁷ Evrard, O. *et al.* Mise en évidence de CaFe_4O_6 et détermination des structures cristallines des ferrites de calcium $\text{CaFe}_{2+n}\text{O}_{4+n}$ ($n = 1, 2, 3$): nouvel exemple d’intercroissance. *J. Solid State Chem.* **35**, 112–119 (1980).
- ⁴⁸ Malaman, B. *et al.* Preparation et caractérisation des ferrites de calcium $\text{CaFe}_{2+n}\text{O}_{4+n}$ a valeurs fractionnaires de n ($3/2, 5/2$) et leur incidence sur le diagramme Fe-Ca-O a 1120 °C. *Mater. Res. Bull.* **16**, 1139–1148 (1981).
- ⁴⁹ Kantor, I. *et al.* BX90: A new diamond anvil cell design for X-ray diffraction and optical measurements. *Rev. Sci. Instrum.* **83**, 125102 (2012).
- ⁵⁰ Kuppenko, I. *et al.* Portable double-sided laser-heating system for Mössbauer spectroscopy and X-ray diffraction experiments at synchrotron facilities with diamond anvil cells. *Rev. Sci. Instrum.* **83**, 124501 (2012).
- ⁵¹ Aprilis, G. *et al.* Portable double-sided pulsed laser heating system for time-resolved geoscience and materials science applications. *Rev. Sci. Instrum.* **88**, 084501 (2017).
- ⁵² Rüffer, R. & Chumakov, A. I. Nuclear resonance beamline at ESRF. *Hyperfine Interact.* **97**, 589–604 (1996).
- ⁵³ Potapkin, V. *et al.* The ^{57}Fe synchrotron Mössbauer source at the ESRF. *J. Synchrotron Radiat.* **19**, 559–569 (2012).
- ⁵⁴ Prescher, C., McCammon, C. & Dubrovinsky, L. MossA: a program for analyzing energy-domain Mössbauer spectra from conventional and synchrotron sources. *J. Appl. Crystallogr.* **45**, 329–331 (2012).

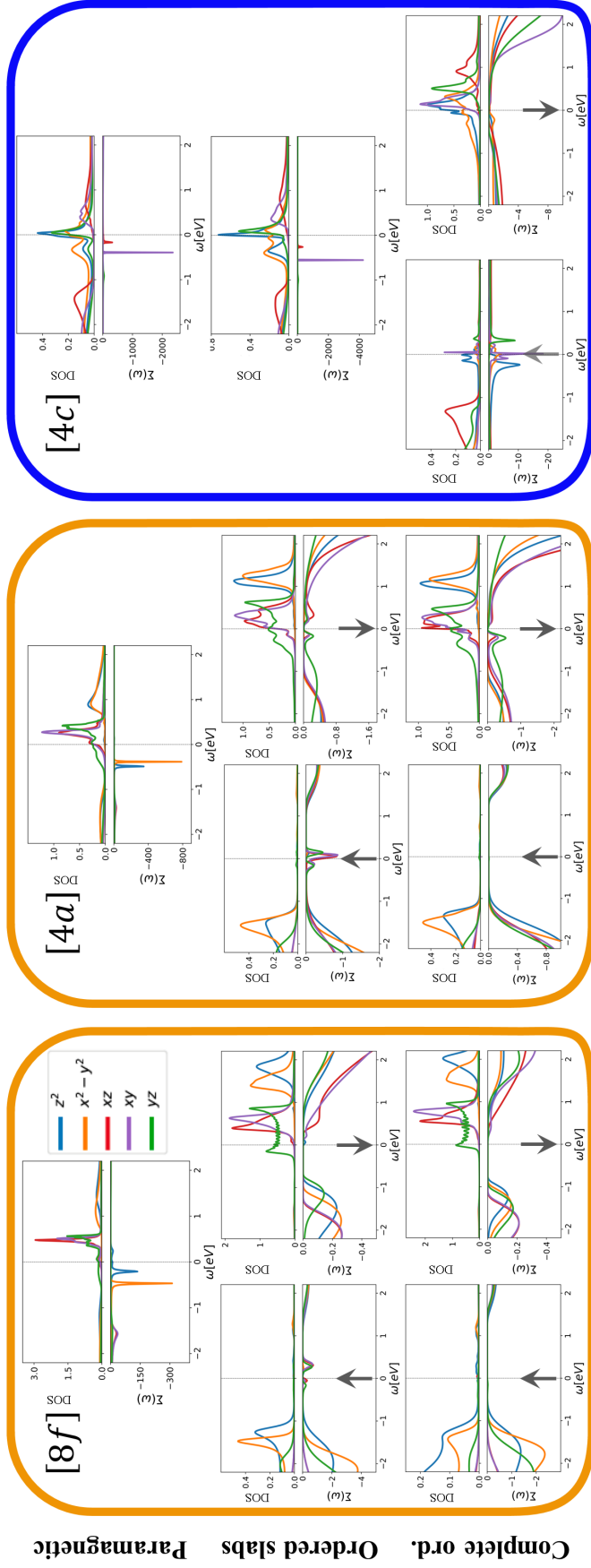
- 55 Menil, F. Systematic trends of the ^{57}Fe Mössbauer isomer shifts in (FeO_n) and (FeF_n) polyhedra. Evidence of a new correlation between the isomer shift and the inductive effect of the competing bond $T - X$ ($\rightarrow\text{Fe}$) (where X is O or F and T any element with a formal positive charge). *J. Phys. Chem. Solids* **46**, 763–789 (1985).
- 56 Vasiukov, D. M. *et al.* Pressure-induced spin pairing transition of Fe^{3+} in oxygen octahedra. *arXiv preprint arXiv:1710.03192v1* (2017).
- 57 Kotliar, G. *et al.* Electronic structure calculations with dynamical mean-field theory. *Rev. Mod. Phys.* **78**, 865 (2006).
- 58 Blaha, P. *et al.* WIEN2k: An APW+lo program for calculating the properties of solids. *J. Chem. Phys.* **152**, 074101 (2020).
- 59 Haule, K., Yee, C.-H. & Kim, K. Dynamical mean-field theory within the full-potential methods: Electronic structure of CeIrIn_5 , CeCoIn_5 , and CeRhIn_5 . *Phys. Rev. B* **81**, 195107 (2010).
- 60 Haule, K. Structural predictions for correlated electron materials using the functional dynamical mean field theory approach. *J. Phys. Soc. Jpn.* **87**, 041005 (2018).
- 61 Haule, K. Exact double counting in combining the dynamical mean field theory and the density functional theory. *Phys. Rev. Lett.* **115**, 196403 (2015).
- 62 Perdew, J. P. & Wang, Y. Accurate and simple analytic representation of the electron-gas correlation energy. *Phys. Rev. B* **45**, 13244 (1992).
- 63 Haule, K. & Birol, T. Free energy from stationary implementation of the DFT+DMFT functional. *Phys. Rev. Lett.* **115**, 256402 (2015).
- 64 Haule, K. Quantum Monte Carlo impurity solver for cluster dynamical mean-field theory and electronic structure calculations with adjustable cluster base. *Phys. Rev. B* **75**, 155113 (2007).
- 65 Momma, K. & Izumi, F. VESTA 3 for three-dimensional visualization of crystal, volumetric and morphology data. *J. Appl. Crystallogr.* **44**, 1272–1276 (2011).
- 66 Foster, P. & Welch, A. Metal-oxide solid solutions. Part 1.—lattice-constant and phase relationships in ferrous oxide (wustite) and in solid solutions of ferrous oxide and manganous oxide. *Trans. Faraday Soc.* **52**, 1626–1635 (1956).

HP-Fe₃O₄

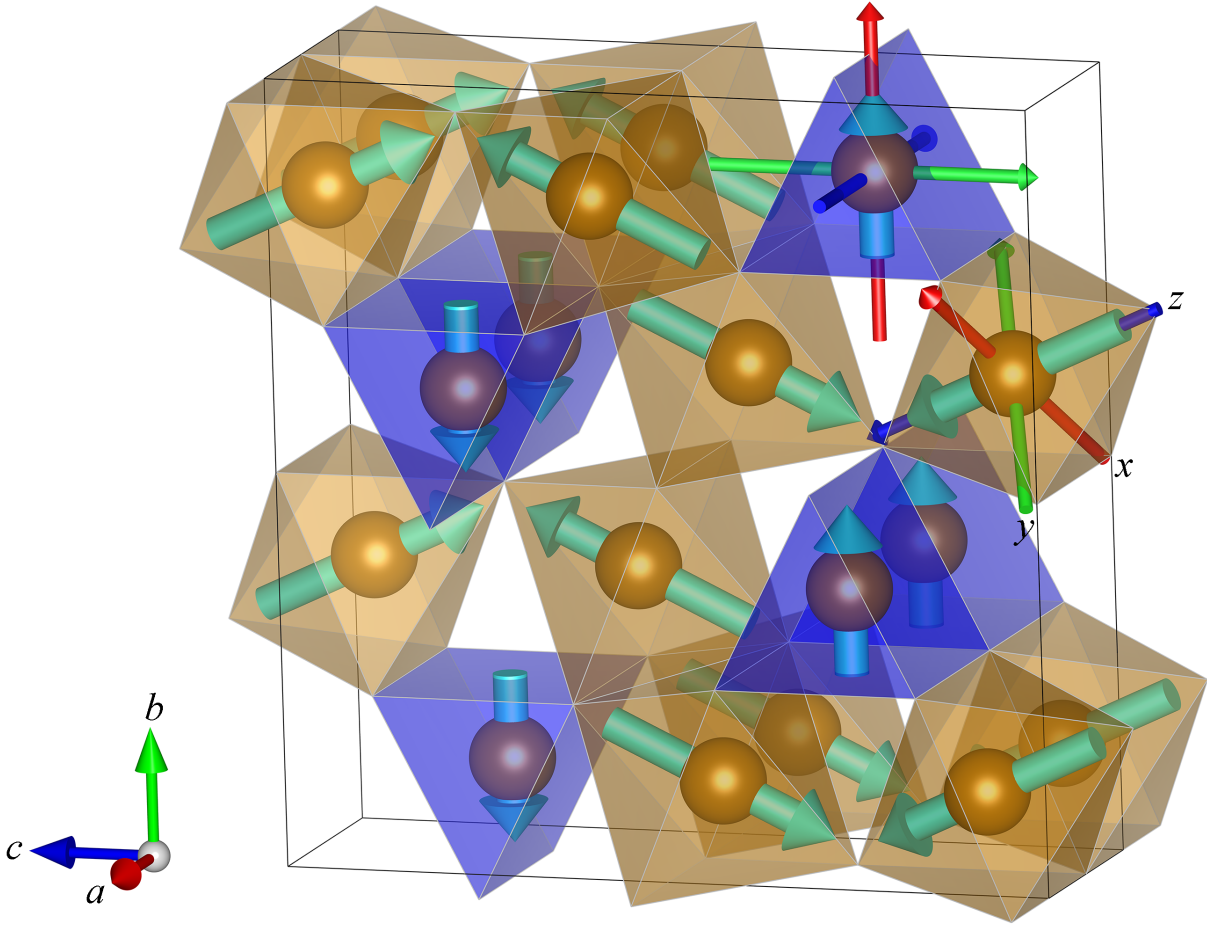


Extended data Fig. 5. Theoretical eDMFT electronic density of states (DOS) and self-energy in HP-Fe₃O₄ for three different states: the paramagnetic state (top row), the intermediate state with ordered slabs and disordered chains (middle row) and the completely ordered state (bottom row). For each state we show the projected electronic DOS on the Fe 3d orbitals in the upper panel, while the lower panel displays the imaginary part of the self-energy, which gives the electronic scattering rate. The plots for the slabs (8f site) and the chains (4c site) are contoured with orange and blue frames, respectively. The up and down arrows mark the spin-majority and spin-minority states, respectively.

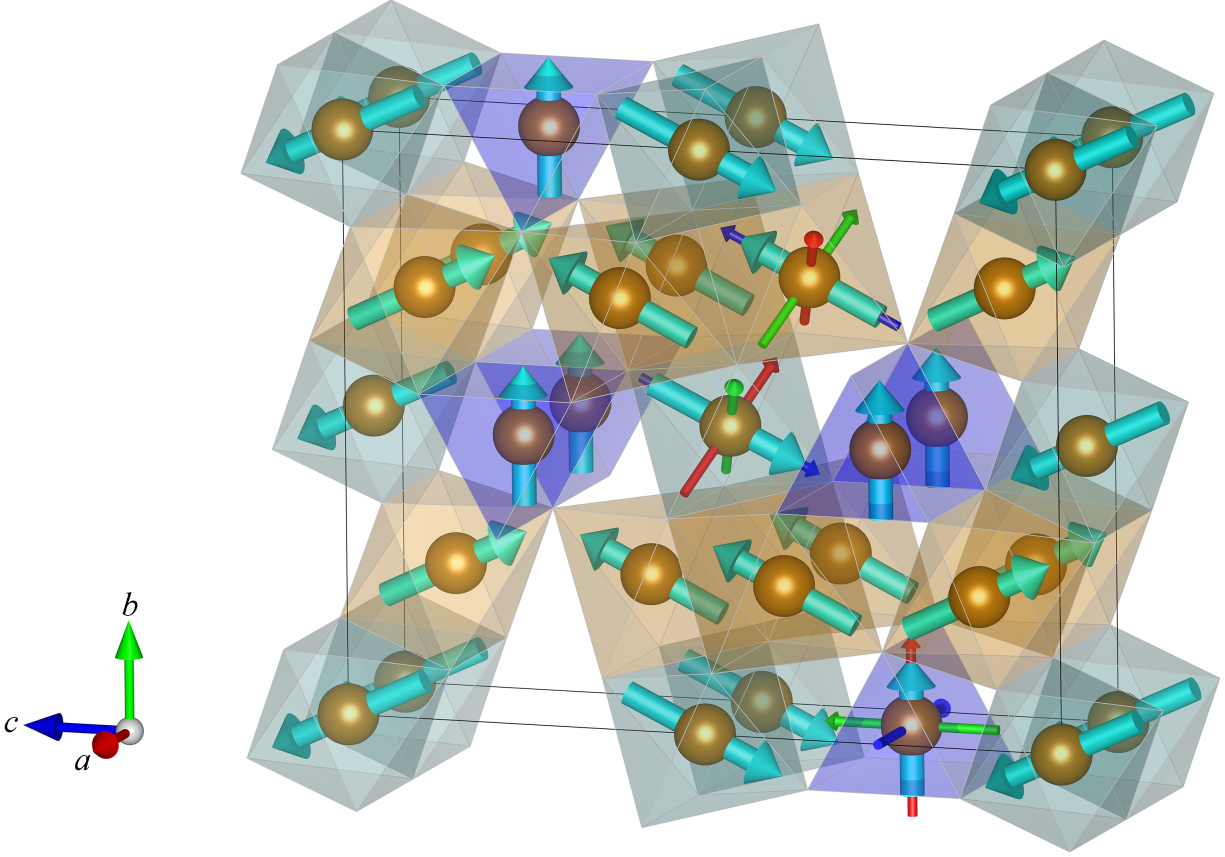
Fe₄O₅



Extended data Fig. 6. Theoretical eDMFT electronic density of states (DOS) and self-energy in Fe₄O₅ for three different states: the paramagnetic state (top row), the intermediate state with ordered slabs and disordered chains (middle row) and the completely ordered state (bottom row). For each state we show the projected electronic DOS on the Fe *3d* orbitals in the upper panel, while the lower panel displays the imaginary part of the self-energy, which gives the electronic scattering rate. The plots for the slabs (*8f* and *4a* sites) and the chains (*4c* site) are contoured with orange and blue frames, respectively. The up and down arrows mark the spin-majority and spin-minority states, respectively.



Extended data Fig. 7. The canted magnetic structure and local coordinate systems used for the eDMFT calculations of HP-Fe₃O₄. The red, green and dark blue axes correspond to the local x , y and z axes, respectively.



Extended data Fig. 8. The canted magnetic structure and local coordinate systems used for the eDMFT calculations of Fe_4O_5 . The red, green and dark blue axes correspond to the local x , y and z axes, respectively, in accord with the previous figure. The light green octahedra correspond to Fe atoms at the $4a$ Wyckoff site.

Extended data Table I. Crystallographic data of the $n\text{FeO}\cdot m\text{Fe}_2\text{O}_3$ homologous series. Among the currently known oxides of this series, two subseries can be distinguished with different type of the slab cycle: an orthorhombic N -family with space group $Cmcm$ and a monoclinic $N,N+1$ -family with space group $C2/m$. The recently discovered Fe_7O_{10} has a more complicated slab cycle. The relevant data of the parent wüstite structure (FeO) are also provided for comparison. The a and b lattice constants of the N -family are equivalent to the b and a lattice constants of the $N,N+1$ -family, respectively.

Compound	SG	Slab cycle	Tr. prism	Iron sites	P, GPa	a , Å	b , Å	c , Å	β	Ref.
<i>N</i> -family										
$\eta\text{-Fe}_2\text{O}_3$	$Cmcm$	1	4c(m2m)	Octahedron 4a(2/m..)	64	2.640	8.639	6.414		[4]
HP- Fe_3O_4	$Cmcm$	2	4c(m2m)	8f(m..)	44	2.694	9.282	9.309		[4]
Fe_4O_5	$Cmcm$	3	4c(m2m)	4a(2/m..) 8f(m..)	ambient	2.891	9.802	12.580	12.965	[19]
Fe_5O_6	$Cmcm$	4	4c(m2m)	8f(m..) 8f(m..)	ambient	2.877	9.917	15.340	15.558	[18]
<i>N,N+1</i> -family										
Fe_5O_7	$C2/m$	1,2	4i(m)	2a(2/m) 4i(m)	41	2.733	9.208	8.270	105.50°	[4]
Fe_7O_9	$C2/m$	2,3	4i(m)	2d(2/m) 4i(m) 4i(m)	ambient	2.895	9.696	11.428	11.916	101.69° [3]
^a Fe_9O_{11}	$C2/m$	3,4	4i(m)	2a(2/m) 4i(m) 4i(m) 4i(m)	ambient	2.892	9.844	14.176	14.480	99.956° [5]
Fe_7O_{10}	$Cmcm$	1,1,2	4c(m2m) 8f(m..)	8f(m..) 8f(m..)	64	2.652	8.767	21.96		[6]
$\text{Fe}_{0.94}\text{O}$	$Fm\bar{3}m$	∞			ambient	^b 3.041	^c 10.084	^d 4.3		[66]

^a Fe_9O_{11} was stabilized as a solid solution with Mg and its actual composition is $\text{Mg}_{0.9}\text{Fe}_{8.1}\text{O}_{11}$ [5].

^b The periodicity along $\langle 110 \rangle$.

^c The periodicity along $\langle 332 \rangle$.

^d The actual cubic lattice constant.

Extended data Table II. Parameters of Mössbauer spectra of the studied high-pressure iron oxides at room temperature. δ_{CS} is the center shift, ΔE_Q is the quadrupole splitting, ε is the quadrupole shift and B_{hf} is the hyperfine magnetic field. The expected octahedral $\text{Fe}^{2+}:\text{Fe}^{3+}$ ratio and calculated center shift values (see Methods section for details) are evaluated assuming that the trigonal prismatic site is occupied only by Fe^{2+} .

Compound	HP-Fe_3O_4		Fe_4O_5		Fe_5O_6		Fe_7O_9	
Tr. prism/oct.	1:2		1:3		1:4		2:5	
Expected oct. $\text{Fe}^{2+}/\text{Fe}^{3+}$ ratio	0:1		1:2		1:1		1:4	
Pressure	20(1) GPa		ambient		ambient		ambient	
	Tr. prism	Oct.	Tr. prism	Oct.	Tr. prism	Oct.	Tr. prism	Oct.
expt. δ_{CS} , mm/s	0.73(2)	0.45(2)	0.98(2)	0.59(1)	0.97(3)	0.70(1)	0.954(3)	0.561(3)
calc. δ_{CS} , mm/s	0.90 ± 0.04	0.30 ± 0.02	0.98	0.57	0.98	0.67	0.98	0.48
$\Delta E_Q/2\varepsilon$, mm/s	2.32(4)	~ 0	2.34(4)	0.44(1)	1.08(4)	0.67(1)	2.736(6)	0.348(4)
B_{hf} , T	0	0	0	24.78(5)	0	32.87(4)	0	0
Area, %	36(5)	64(5)	21(4)	79(4)	19(2)	81(2)	26.9(6)	73.1(6)

Extended data Table III. Theoretical eDMFT electric conductivity σ at 100 K, occupation n_d and magnetic moment M for each Fe-site in HP-Fe₃O₄ and Fe₄O₅. Here σ^b and σ^c are the conductivities along the b and c axes, respectively, while σ^a corresponds to the a axis, i.e. along the 1D chains. The slabs of Fe₄O₅ have another Fe-site at the $4a$ Wyckoff position, in addition to the $8f$ position.

Compound	Magnetic order	σ , $10^5 \cdot \text{S/m}$			Fe occupation n_d ($4c$, $8f$, [$4a$])	Magn. moment, μ_B ($4c$, $8f$, [$4a$])
		σ^a	σ^b	σ^c		
HP-Fe ₃ O ₄	<i>Complete ordering</i>	55	17	25	(5.80 , 5.58)	(4.12 , 4.28)
	<i>Ordered slabs</i>	2.4	2.0	2.3	(5.80 , 5.57)	(0 , 4.28)
	<i>Paramagnetic</i>	1.2	1.1	0.9	(5.80 , 5.57)	(0 , 0)
Fe ₄ O ₅	<i>Complete ordering</i>	5.0	3.0	3.0	(5.83 , 5.80 , 5.51)	(3.44 , 4.08 , 4.4)
	<i>Ordered slabs</i>	2.2	2.3	2.4	(5.90 , 5.76 , 5.58)	(0 , 4.06 , 4.34)
	<i>Paramagnetic</i>	1.9	1.5	1.6	(5.92 , 5.72 , 5.61)	(0 , 0 , 0)

Extended data Table IV. Variations of the conductivity and its anisotropy in HP-Fe₃O₄ on electronic doping in the completely ordered magnetic state. The discrepancy in conductivity values with Extended Data Table III is due to the use of a less dense mesh in these calculations.

Doping, electron per formula unit	Conductivity, S/m		
	σ^a	σ^b	σ^c
+0.09	30.6	16.1	16.4
+0.06	115.0	37.1	34.8
0	43.5	15.0	28.5
-0.05	15.0	5.2	6.3
-0.07	25.6	5.9	5.4